Interplay Between Kinetic Inductance, Nonlinearity, and Quasiparticle Dynamics in Granular Aluminum Microwave Kinetic Inductance Detectors

Francesco Valenti,[1,2] Fabio Henriques,[1] Gianluigi Catelani,[3] Nataliya Maleeva,[1] Lukas Grünhaupt,[1] Uwe von Lüpke,[1] Sebastian T. Skacel,[4] Patrick Winkel,[1] Alexander Bilmes,[1] Alexey V. Ustinov,[1,5] Johannes Goupy,[6] Martino Calvo,[6] Alain Benoît,[6] Florence Levy-Bertrand,[6] Alessandro Monfardini,[6] and Ioan M. Pop[1,4,*]

[1] *Physikalisches Institut, Karlsruhe Institute of Technology, 76131 Karlsruhe, Germany*
[2] *Institut für Prozessdatenverarbeitung und Elektronik, Karlsruhe Institute of Technology, 76344 Eggenstein-Leopoldshafen, Germany*
[3] *JARA Institute for Quantum Information (PGI-11), Forschungszentrum Jülich, 52425 Jülich, Germany*
[4] *Institute of Nanotechnology, Karlsruhe Institute of Technology, 76344 Eggenstein-Leopoldshafen, Germany*
[5] *Russian Quantum Center, National University of Science and Technology MISIS, 119049 Moscow, Russia*
[6] *Université Grenoble Alpes, CNRS, Grenoble INP, Institut Néel, 38000 Grenoble, France*

(Received 9 November 2018; revised manuscript received 8 March 2019; published 31 May 2019)

Microwave kinetic inductance detectors (MKIDs) are thin-film, cryogenic, superconducting resonators. Incident Cooper pair-breaking radiation increases their kinetic inductance, thereby measurably lowering their resonant frequency. For a given resonant frequency, the highest MKID responsivity is obtained by maximizing the kinetic inductance fraction α. However, in circuits with α close to unity, the low supercurrent density reduces the maximum number of readout photons before bifurcation due to self-Kerr nonlinearity, therefore setting a bound for the maximum α before the noise-equivalent power (NEP) starts to increase. By fabricating granular aluminum MKIDs with different resistivities, we effectively sweep their kinetic inductance from tens to several hundreds of pH per square. We find a NEP minimum in the range of 30 aW/$\sqrt{\text{Hz}}$ at $\alpha \approx 0.9$, which results from a trade-off between the onset of nonlinearity and a nonmonotonic dependence of the noise spectral density versus resistivity.

DOI: 10.1103/PhysRevApplied.11.054087

I. INTRODUCTION

Since their first implementation 15 years ago [1], microwave kinetic inductance detectors (MKIDs) have played an important role in ground-based radioastronomy [2–7], particle detection [8–12], and are promising candidates for spaceborne millimeter wave observations [13–16]. This remarkable development was facilitated by the technological simplicity of MKIDs, which consist of thin-film, cryogenic, superconducting resonators in the microwave domain. The MKID signal is the shift of its resonant frequency due to an increase in the kinetic inductance of the film, which is itself proportional to the number of Cooper pairs (CP) broken by the incoming radiation. These compact, low-loss and multiplexable detectors can also provide a convenient tool to probe material properties, such as the change of dielectric constant due to a superfluid transition [17], the density of states of granular aluminum and indium oxide [18], or to image phonons [19,20].

The first MKIDs consisted of thin-film-aluminum distributed-element resonators. Their numerous incarnations now include lumped-element- (LE) resonator geometries [21], solutions such as spiral resonators [22] or various kinds of antenna coupling [23–25], and a wealth of different film materials such as TiN [26–28], NbN [29], PtSi [30], and W_xSi_y [31], including hybrid realizations [32] and multilayered films [33–36].

Here, we propose granular aluminum (grAl), a composite material made of pure Al grains with median size of the order of $a = 3 \pm 1$ nm in an aluminum oxide matrix [37,38], as an alternative material for MKIDs. As illustrated in Fig. 1, we employ a coplanar-waveguide (CPW) geometry, in which the ground plane and the feedline of the CPW are made of pure aluminum, 50 nm thick, and the lumped-element MKID resonators are entirely made of grAl.

Granular aluminum is an appealing material because it already demonstrated high microwave internal quality factors, from 10^5 at low photon number up to 10^6 in the strong drive regime [39–41], and ease of fabrication, which simply consists in aluminum deposition in a controlled

*ioan.pop@kit.edu

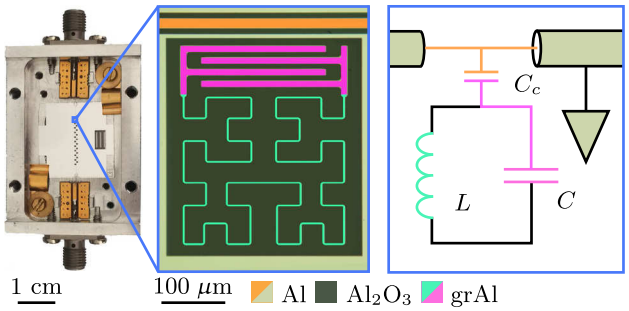

FIG. 1. Optical images of the aluminum sample holder and a grAl lumped-element resonator, together with its equivalent circuit. A sample consists of an ensemble of 22 resonators coupled to a central coplanar microwave waveguide, which is used to perform transmission spectroscopy. The enlargement shows a single resonator, where we highlight the interdigitated capacitor in magenta (which gives both C and C_c) and the meandered inductor (which gives L) in green. The sapphire substrate is shown in dark green. All resonators are fabricated from a 20-nm-thick grAl film using e-beam liftoff lithography, while the central conductor of the coplanar waveguide (orange) and the ground plane (light green) are made of 50-nm-thick aluminum patterned by optical liftoff. The meandered inductor for samples A–D is shaped as a third-degree Hilbert curve (shown), while for samples E and F it is shaped as a second-degree Hilbert curve (cf. text and Appendix A). In order to distribute the resonant frequencies $f_0 = (2\pi\sqrt{LC})^{-1}$ of the 22 resonators, we sweep the capacitances by changing the length of the interdigitated fingers.

oxygen atmosphere [37,38]. Furthermore, by varying the oxygen pressure during deposition, one can tune material parameters such as the resistivity (from 1 to 10^4 $\mu\Omega$ cm), kinetic inductance, and superconducting gap. The kinetic inductance of a square of thin film is determined by the ratio of the normal-state sheet resistance per square R_n and the critical temperature T_c [42,43]:

$$L_{\mathrm{kin},\square} = \frac{0.18\hbar}{k_B}\frac{R_n}{T_c}, \tag{1}$$

and, in the case of grAl, it can reach values as high as a few nH/$\square$ [40,41]. Equation (1) is valid under the assumption of the grAl BCS constant being reasonably close to 1.76, which holds for resistivities up to the mΩ cm regime [44–46]. The grAl microstructure, consisting of superconducting grains separated by thin insulating shells, can be modeled as a network of Josephson junctions (JJs), which simplifies to a one-dimensional (1D) JJ chain for resonators in the thin-ribbon limit (length $\gg$ width $\gg$ thickness) [47]. We can use this model to quantitatively estimate the nonlinearity of grAl resonators and extract the self-Kerr coefficient of the fundamental mode K_{11} [47], similarly to the case of resonators made of mesoscopic JJ arrays [48–50].

This article is organized as follows: in Sec. II, we propose a model to quantify the interplay between kinetic inductance fraction, nonlinearity and quasiparticle dynamics, and its effect on the noise-equivalent power (NEP)—the main operational figure of merit of MKIDs. We discuss experimental methods and results in Sec. III, showing that we can exploit the tunability of the grAl nonlinearity and superconducting gap to achieve low NEP values. In Sec. IV we conclude by proposing guidelines to further reduce the NEP in future designs.

II. THEORY

The NEP is defined as the radiant power needed to have equal signal and noise amplitudes in a 1-Hz output bandwidth, and can be expressed as [33]

$$\mathrm{NEP} = \frac{S}{\mathfrak{R}}, \tag{2}$$

where S is the noise spectral density (Sec. II A) and $\mathfrak{R}$ is the responsivity (Sec. II C). In the following subsections, we discuss in detail the influence of grAl parameters on each of these two quantities.

A. Noise spectral density

Fluctuations of the MKID resonant frequency in the absence of incoming radiation constitute noise. The noise spectral density (NSD) is computed by recording the fluctuations of the resonant frequency over time, taking its Fourier transform and dividing by the square root of the output bandwidth, hence the NSD is quoted in Hz/$\sqrt{\mathrm{Hz}}$ units (cf. Appendix B). These fluctuations can be either dominated by the added noise of the measurement setup, or by noise sources intrinsic to the resonator, such as dielectric two-level systems [51], microscopic charge fluctuators [52], or fluctuations in the number of quasiparticles (QPs) [53–55]. As discussed in Sec. III C, for the grAl MKIDs in this work the latter mechanism appears to be dominant, and reducing the QP density can be a fruitful approach to suppress the NSD.

B. Phonon trapping and quasiparticle fluctuations

The grAl MKIDs are surrounded by the comparatively much larger aluminum ground plane (cf. Fig. 1), which has a lower superconducting gap and can act as a phonon trap [56–58], possibly reducing the number of QPs generated by nonthermal phonons from the substrate, as schematically illustrated in Fig 2. In the following, we develop a theoretical framework to quantify the phonon-trapping effect of the ground plane, i.e., how the difference between superconducting gaps of the circuit and ground plane is related to a suppression of the QP generation-recombination noise, and with that, the NEP. In order to model the effect of phonon traps, we start from the expression of the NEP (in the ideal case of unit conversion

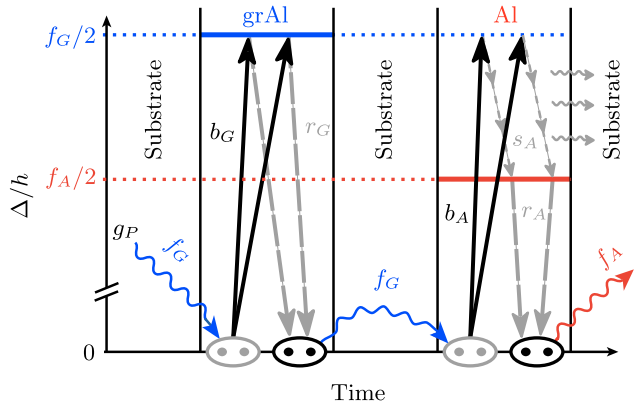

FIG. 2. Phonon trapping and quasiparticle number reduction: schematic depiction of the dynamics described in Eqs. (4)–(6). We show the superconducting energy band diagram in the excitation picture for both grAl (in blue) and Al (in red). Excitations and relaxations are represented by solid black and dashed gray arrows, respectively. Wiggly arrows represent phonons and the labels represent their corresponding frequency. Substrate phonons with characteristic frequency larger than the grAl spectral gap f_G, generated at rate g_P, can break grAl CPs at rate b_G. The resulting grAl QPs recombine at rate r_G, emitting phonons that can travel through the substrate and reach the Al ground plane, which covers most of the chip (cf. Fig. 1), breaking Al CPs at rate b_A. The excited QPs can scatter to a lower energy via electron-phonon interaction at rate s_A and recombine to form an Al CP at rate r_A. In both cases the emitted phonons have characteristic frequencies lower than the spectral gap of grAl, thus being unable to break grAl CPs.

efficiency) dominated by QP generation-recombination noise [54,55],

$$\mathrm{NEP} = 2\Delta_G\sqrt{\frac{N_G}{\tau_G}}, \tag{3}$$

where Δ_G, N_G, and τ_G are the grAl superconducting gap, QP number, and QP lifetime, respectively. In the following we use the indexes G and A to refer to thin-film grAl and aluminum. We assume that all phonons in grAl, Al, and the substrate quickly reach the steady state after a high-energy generation event [19,20], allowing us to describe their density as position independent. Moreover, since the temperature T is small ($1.76k_BT \ll \Delta_G$, Δ_A, $\Delta_G - \Delta_A$), we neglect any effect of thermal phonons and we focus on phonons with energy above the highest grAl gap ($E_P > \Delta_G^{\max}$), so they can create quasiparticles in grAl by breaking Cooper pairs at a rate b_G independent of Δ_G. We indicate with N_P the number of these "hot" phonons. In addition to quasiparticles in grAl with number N_G, we also have quasiparticles in Al.

We are interested in the quasiparticles generated by hot phonons. They can recombine by emitting a hot phonon again, or scatter by emitting lower-energy phonons that cannot break pairs in grAl (cf. Fig. 2). We model the dynamics of hot phonons and quasiparticles in a phenomenological way, with rate equations of the Rothwarf-Taylor type. For quasiparticles in grAl, the relevant processes are generation from pair breaking by hot phonons (rate b_G) and recombination (rate r_G). Similarly, for quasiparticles in Al, we have generation by pair breaking (b_A) and recombination (r_A), but also scattering to lower energies (rate s_A). For the phonons, we assume some generation mechanism with rate g_P, in addition to generation and recombination in both grAl and Al. The rate equations are then

$$\dot{N}_G = -2r_GN_G^2 + 2b_GN_P, \tag{4}$$

$$\dot{N}_A = -2r_AN_A^2 + 2b_AN_P - s_AN_A, \tag{5}$$

$$\dot{N}_P = g_P - b_AN_P + r_AN_A^2 - b_GN_P + r_GN_G^2. \tag{6}$$

We consider now the steady-state solution. The first equation simply gives

$$N_G = \sqrt{\frac{b_GN_P}{r_G}} \tag{7}$$

and the last two terms in the last equation cancel out. Then we are left with the system

$$0 = -2r_AN_A^2 + 2b_AN_P - s_AN_A, \tag{8}$$

$$0 = g_P - b_AN_P + r_AN_A^2. \tag{9}$$

We can solve the first equation for N_A in terms of N_P, substitute into the second equation, and find

$$N_P = \frac{g_P}{b_A} + \frac{4r_Ag_P^2}{b_As_A^2}. \tag{10}$$

For "weak" scattering, $s_A \ll 2\sqrt{r_Ag_P}$, we then have

$$N_P \approx \frac{4r_Ag_P^2}{b_As_A^2}. \tag{11}$$

Note that Eq. (11) diverges as the scattering rate decreases. This unphysical result is due to the fact that we neglect other mechanisms that can decrease the hot phonon number, for example, escape from the substrate into the sample holder, or phonon scattering that cools them below the grAl gap. In a relaxation-time approach, such a contribution would add a term $-e_PN_P$ to the right-hand side of Eq. (6) in order to account for escaped phonons. Then we can show that Eq. (11) remains valid so long as $4e_P/b_A \ll s_A^2/4r_Ag_P$.

Having N_P from Eq. (11), we can calculate N_G using Eq. (7). As for the quasiparticle lifetime, linearizing Eq. (4)

around the steady state, one can see that $1/\tau_G = 4r_G N_G$. Therefore, from Eq. (3) we get

$$\mathrm{NEP} \approx 4\Delta_G\sqrt{b_G N_P} = 8g_P\sqrt{\frac{b_G r_A}{b_A}}\frac{\Delta_G}{s_A}. \tag{12}$$

The quasiparticle scattering rate s_A depends on the quasiparticle energy ϵ above the gap Δ_A. At low temperature, we approximate the scattering rate due to electron-phonon interaction by its zero-temperature expression, which according to Ref. [59] can be written in the form:

$$s_A = \frac{1}{\tau_{0A}\Delta_A^3}\int_0^{\epsilon} d\omega\,\omega^2 \frac{\Delta_A + \epsilon - \omega}{\sqrt{(\Delta_A + \epsilon - \omega)^2 - \Delta_A^2}} \times\left[1 - \frac{\Delta_A^2}{(\Delta_A + \epsilon)(\Delta_A + \epsilon - \omega)}\right], \tag{13}$$

where the prefactor $1/\tau_{0A}$ accounts for the strength of the electron-phonon interaction. For $\epsilon \lesssim \Delta_A$ we then find $s_A \propto (\epsilon/\Delta_A)^{7/2}(1 + \epsilon/8\Delta_A)/(1 + \epsilon/\Delta_A)$, while for $\epsilon \gg \Delta_A$ we have $s_A \propto (\epsilon/\Delta_A)^3$. Here $\epsilon \approx \Delta_G - \Delta_A$ is of order Δ_A, so the first expression applies. Since we are interested in the dependence of NEP on Δ_G, dropping prefactors we arrive at

$$\mathrm{NEP} \propto \Delta_G^2\left(\frac{\Delta_A}{\Delta_G - \Delta_A}\right)^{7/2}\frac{1}{\Delta_G + 7\Delta_A}. \tag{14}$$

Equation (14) indicates an anticorrelation between the NEP and the superconducting gap Δ_G. We recall that Eq. (14) applies only for the case of a system in which the ground plane has a relevant phonon-trapping effect, i.e., $\Delta_G - \Delta_A \gg 1.76k_BT$, otherwise it would imply an unphysical divergence of the NEP when resonators and ground plane are fabricated with the same material. In Sec. III C we present experimental results, which are qualitatively consistent with this phonon-trapping model, and we show that the increase of the grAl gap at the top of the so-called superconducting dome [37,38,44–46,60–62] is responsible for a significant improvement in detector performance.

C. Responsivity

The responsivity of a MKID can be expressed as [33]

$$\mathfrak{R} = \frac{|\delta f_0|}{P_{\mathrm{abs}}} = \frac{\alpha f_0}{4}\frac{\delta x_{\mathrm{QP}}}{P_{\mathrm{abs}}}, \tag{15}$$

where δf_0 is the shift in resonant frequency due to pair breaking, P_{abs} is the radiant power absorbed by the detector, α is the kinetic inductance fraction with respect to the total inductance, f_0 is the unperturbed resonant frequency, and δx_{QP} is the shift in the quasiparticle density, defined as twice the fraction of broken CPs. For practical reasons, the choice of values for the operational frequencies f_0 is limited by the availability and cost of readout electronics, and it is typically in the range of a few GHz.

To estimate P_{abs}, we assume that every collected photon with $hf > 2\Delta$ breaks a CP. The amount of impedance matching between the resonator plane and the medium through which the photons propagate (for example, vacuum or dielectric substrate) defines the detector absorptance $\mathcal{A}$ (cf. Appendix A). The power absorbed by the resonators is then $P_{\mathrm{abs}} = \delta P_{\mathrm{in}}\mathcal{A}$, where δP_{in} is the change in radiant power under illumination through the optical setup. Under operational conditions, for any MKID design, one aims to minimize the impedance mismatch for the incoming radiation, in order to obtain a value for $\mathcal{A}$ as close as possible to unity.

D. Voltage responsivity

Following Eq. (15), the responsivity $\mathfrak{R}$ scales linearly with the kinetic inductance fraction α. However, in the limit $\alpha \to 1$ the performance of MKIDS is limited by the early onset of nonlinear phenomena, i.e., the resonators bifurcate at low readout voltages. In order to maximize the microwave signal-to-noise ratio, one wants to operate MKIDs at the highest possible readout power before bifurcation [47,63,64] and before degrading the detector by breaking CPs [65–67]. Typically, in high-kinetic-inductance detectors, bifurcation sets the maximum number of circulating photons, which in our case is in the range of $10^5 - 10^6$ (cf. Fig. 3), and can be as low as 10^2, as reported in Ref. [41]. The NEP defined in Eq. (2) is thus *implicitly* dependent on the maximum microwave readout voltage, which in turn scales with the square root of the maximum number of circulating photons before bifurcation n_{max}. This dependence can be made explicit by defining a *voltage responsivity*

$$\mathfrak{R}_V \equiv \alpha\sqrt{n_{\mathrm{max}}}. \tag{16}$$

The voltage responsivity is trivially zero if α is zero, but it also vanishes in the limit $L_{\mathrm{kin}} \to \infty$ ($\alpha \to 1$), when the resonator nonlinearity also increases, suppressing n_{max}. In the following, we quantify this nonmonotonic dependence.

The kinetic inductance fraction $\alpha = L_{\mathrm{kin}}/L_{\mathrm{tot}}$ can be estimated by knowing the geometry, resistivity, and critical temperature of a resonator, as we discuss in Appendix C. We show that for a grAl lumped-element resonator with kinetic inductance dominating over the geometric inductance we can write (cf. Appendix D)

$$n_{\mathrm{max}} = \frac{4\ell^2\hbar\sqrt{C}}{3\sqrt{3}Q_c(\pi ea)^2\sqrt{L_{\mathrm{kin}}}}, \tag{17}$$

where ℓ is the meandered inductor length and C is the interdigitated capacitance (cf. Fig. 1), Q_c is the coupling quality

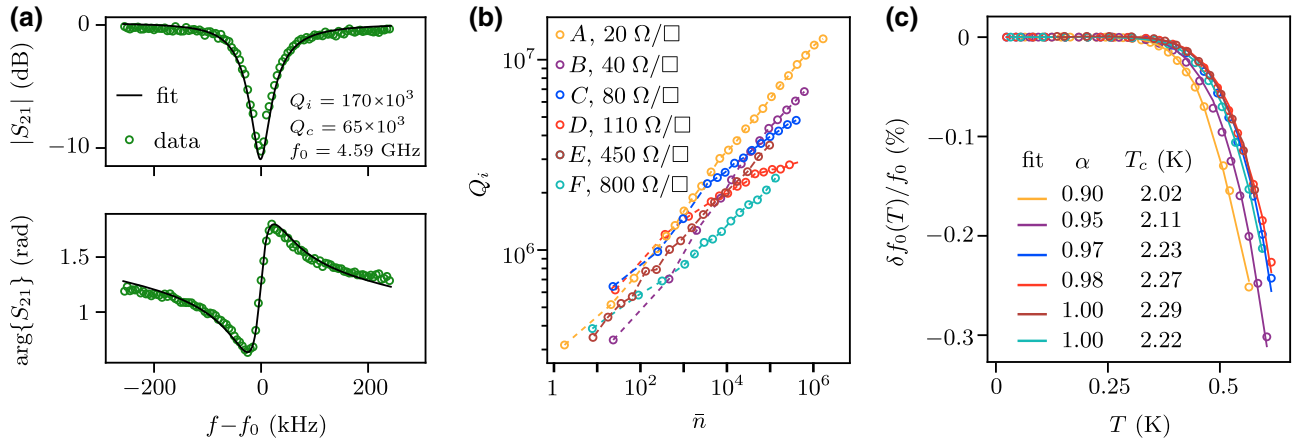

FIG. 3. Microwave characterization of MKIDs via transmission measurements. (a) Amplitude (normalized by the sample-holder response) and phase of the transmission coefficient S_{21} for a resonator in sample A, at a readout power in the single-photon regime ($\bar{n} \approx 1$). Raw data is shown as green circles and the solid black line is the fit to the complex scattering parameters from Ref. [68]; the fitted values are given in the top panel. (b) Internal quality factors as a function of the average number of readout photons circulating in the resonator, shown up to the bifurcation threshold $\bar{n} = n_{\max}$ in log-log scale for all samples. The average photon number is calculated from the estimated on-chip readout power as $\bar{n} = 2Q_c P_{\text{cold}}/\hbar\omega_0^2$ (cf. Appendix D). The single-photon regime corresponds to $P_{\text{cold}} \approx -150$ dBm. Notice that the maximum photon number decreases for higher resistivity films, due to the higher nonlinearity [cf. Eq. (17)]. (c) Change in resonant frequency as a function of temperature, averaged for all resonators in each sample [colored circles, using the same palette as in (b)]. We fit the measured values with the BCS equation $\delta f_0(T)/f_0 = -3.32\alpha\sqrt{T_c/T}\exp(1.76T_c/T)$, adapted from Ref. [69] (colored lines), where we use $f_0 = f_0(T \approx 25$ mK). The fitting parameters are the kinetic inductance fraction α and the critical temperature T_c, shown in the legend.

factor, e is the electron charge, and a is the size of an aluminum grain. By plugging α and Eq. (17) into Eq. (16) one finds

$$\mathfrak{R}_V \sim \frac{L_{\text{kin}}^{3/4}}{L_{\text{kin}} + L_{\text{geom}}}, \tag{18}$$

with $L_{\text{kin}} \sim R_n/T_c$ [cf. Eq. (1)], where R_n is the normal-state sheet resistance per square, and T_c is the critical temperature. From Eq. (18) one can see that $\mathfrak{R}_V$ tends to zero for both limit cases $L_{\text{kin}} = 0$ (no detection) and $L_{\text{kin}} \to \infty$ (fully nonlinear system). The voltage responsivity increases sharply with L_{kin} until it reaches a maximum at $\alpha = 3/4$, after which it slowly decreases (cf. Fig. 4). Thus, $\mathfrak{R}_V$ quantifies the interplay between kinetic inductance and nonlinearity, and is a convenient metric to determine whether a given kinetic inductance fraction α gives a sensitive enough detector, while not being severely limited by nonlinearity.

III. EXPERIMENTAL RESULTS

A. Measurement setups

The MKIDs discussed in this work are lumped-element resonators, composed of a meandered inductor shaped as a Hilbert curve of third or second degree (H3 and H2), and an interdigitated capacitor (cf. Appendix A). The 20-nm-thick grAl film is patterned on a sapphire substrate via e-beam liftoff lithography. We fabricate 2×2 cm^2 chips hosting 22 resonators each. We label the chips from A to F according to the grAl sheet resistance, of 20, 40, 80, 110, 450, 800 Ω/□, respectively. The reader may refer to Appendix E for more details on the material properties of the fabricated samples. The 50-nm-thick surrounding Al CPW ground plane is patterned in a second optical liftoff lithography step.

Two different measurement setups are required in order to characterize (a) the intrinsic properties of the MKID resonators, at frequencies in the GHz range, and (b) the operational MKID response to millimeter wave radiation. To measure their microwave properties, we anchor the MKIDs to the base plate of a so-called "dark" dilution cryostat, with a base temperature of about 25 mK. In this setup, we couple to room temperature electronics via heavily attenuated and filtered radio-frequency (rf) lines, including IR filters (cf. Ref. [78]), with the goal of reducing stray radiation from the higher temperature stages of the cryostat.

On the other hand, in order to measure the NEP, we need to shine millimeter wave radiation onto the resonators and operate them at high readout powers. We thus use a much less shielded dilution refrigerator, with an optical opening and a base temperature of approximately 150 mK, which we refer to as the "optical" cryostat. The sample chip is mounted in an aluminum box with an optical window on one side (cf. Fig. 1 and Appendix F). For measurements performed in the optical cryostat, the optical window is facing a cryogenic millimeter wave optical

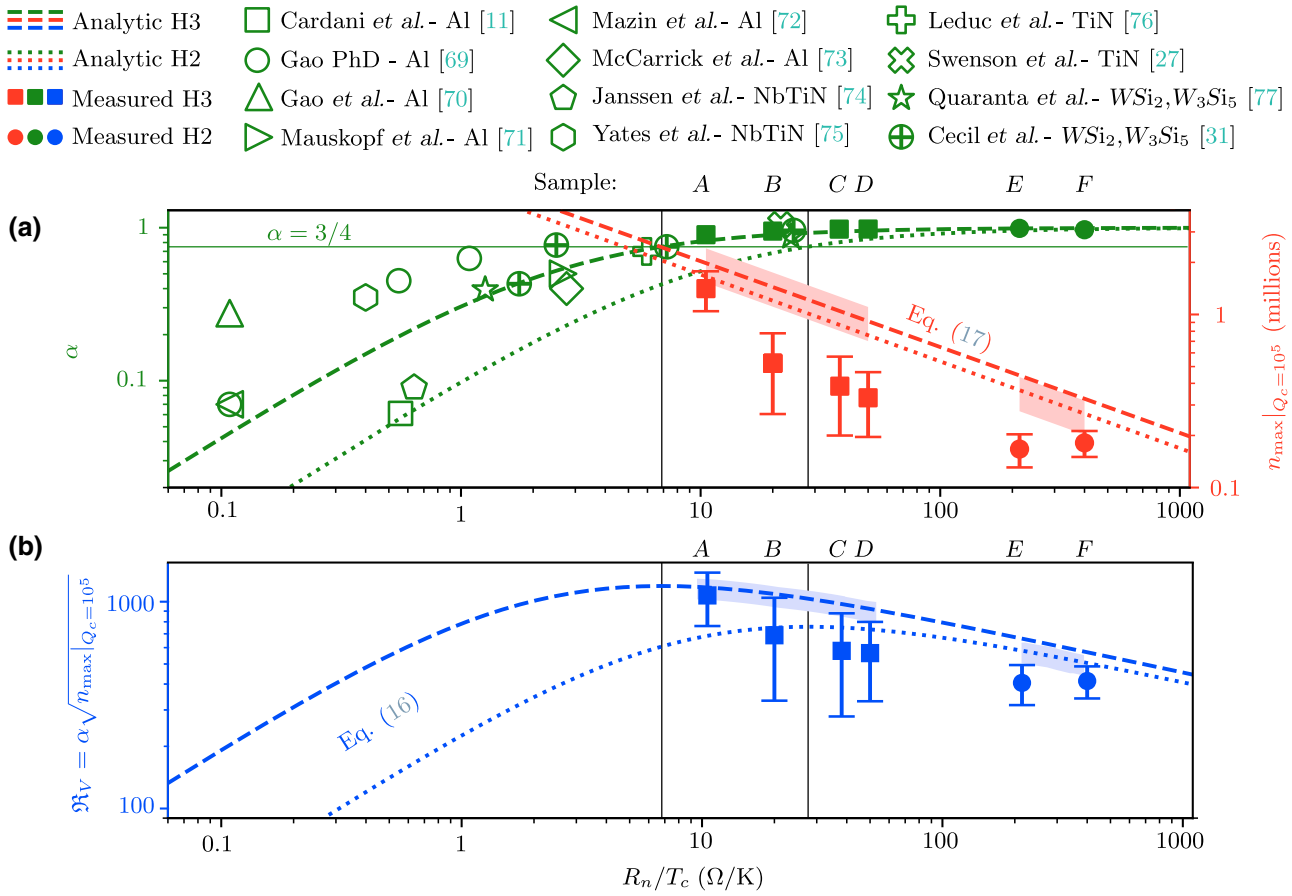

FIG. 4. Kinetic inductance fraction, maximum number of readout photons, and voltage responsivity as a function of the sheet resistance per square R_n scaled to the critical temperature T_c. (a) We plot the kinetic inductance fraction α in green and the maximum number of readout photons before bifurcation $n_{\max}$ in red. Dashed and dotted lines are analytical predictions for H3 and H2 geometries used in this work, for both α (cf. Appendix C) and $n_{\max}$ [estimated with Eq. (17) at a fixed $Q_c = 10^5$]. The color shaded regions overlapping with the $n_{\max}$ analytical lines represent the range of maximum photon number values corresponding to the different interdigitated capacitances C of the various resonators in each sample [cf. Eq. (17)]. Full markers show values measured in this work: squares and circles relate to H3 and H2 geometries, respectively. For comparison, empty markers show α values reported in the literature for various materials (cf. Refs. [11,27,31,69–77] and Appendix C). The measured $n_{\max}$ values are approximately two times lower than predicted for all samples, which might be due to a systematic underestimation of the on-sample readout power. The reported values are averaged over all functional resonators for each sample. (b) Voltage responsivity $\mathfrak{R}_V$, defined as the product between the kinetic inductance fraction α and the square root of the maximum number of readout photons before bifurcation $n_{\max}$ [cf. Eq. (16)]. We report values for H3 and H2 geometries with dashed and dotted lines (analytical predictions) and square and circle markers (measured data), respectively. The color shaded regions overlapping with the lines represent the range of different interdigitated capacitances C. The maximum voltage responsivity is obtained at $\alpha = 3/4$ [cf. (a)], as indicated by the vertical black lines across the two panels (left line for H3 geometry, right line for H2).

setup used to focus the blackbody radiation onto the sample, as described in Ref. [33]. For measurements performed in the dark cryostat, the optical window is covered with aluminum tape, and the sample holder is placed in a series of successive cryogenic infrared and magnetic shields, similar to Ref. [78].

B. Microwave characterization

Figure 3 shows the results of measurements performed in the dark cryostat. In Fig. 3(a) we show a typical result for the transmission coefficient S_{21} in the vicinity of the resonant frequency of one of the MKIDs in sample A, for a readout power in the single-photon regime. We employ the circle fit routine detailed in Ref. [68] to extract resonator parameters of interest, namely the resonant frequency f_0, the internal quality factor Q_i, and the coupling quality factor Q_c. An example of fitted on-resonance frequency response is shown in Fig. 3(a), from which we extract an internal quality factor on the order of 10^5 in the single-photon regime.

In order to compute the average number of readout photons in the resonator, $\bar{n}$, we estimate the on-chip power

by summing the total attenuation on the input line of the cryostat (see Appendix G). It is important to note that, due to the uncertainty in the attenuation figure of the rf components over a broad frequency range, this method is only accurate within an order of magnitude. In Fig. 3(b) we present measurements of Q_i as a function of $\bar{n}$, for readout powers ranging from $\bar{n} \approx 1$ up to the critical number of readout photons n_{max} [reported in Fig. 4(a) along with its analytical calculation], at which the resonator bifurcates. The internal quality factor increases monotonically with the average number of photons in the resonators. This type of dependence was previously observed for grAl resonators in Ref. [41], and it is also routinely measured in thin-film aluminum resonators [51]. The increase of the internal quality factor with power can be interpreted as the combined effect (cf. Fig. 2(c) from Ref. [41]) of the saturation of dielectric losses [51,79], together with photon-assisted unpinning of nonequilibrium QPs, which are then allowed to either diffuse away from regions of high current density or to recombine into CPs [80,81].

By sweeping the sample temperature up to about 600 mK we observe a downward shift in the resonant frequency, as shown in Fig. 3(c), which we fit using a BCS model [69] to obtain the kinetic inductance fraction α and the critical temperature T_c. In the inset of Fig. 3(c), we report the resulting fit parameters averaged over all functional resonators in each chip. The obtained α is in good agreement with the analytical prediction [cf. Fig. 4(a)], and T_c shows a dome-shaped dependence with resistivity [cf. Figs. 3(c) and 5(d)] in agreement with Refs.[37,38,44–46,60–62].

Using the model of Eq. (17) for the maximum number of circulating photons before bifurcation, in Fig. 4(a) we plot the calculated n_{max} and α versus the ratio of the normal-state sheet resistance and critical temperature, R_n/T_c, which determines the kinetic inductance [see Eq. (1)]. For comparison, in Fig. 4(a) we also overlay the measured values of α and n_{max} for samples A–F, together with a literature survey of reported α values for superconducting resonators fabricated with various other materials.

By replacing the expressions of α and n_{max} in Eq. (16), we can compare analytical predictions of the voltage responsivity $\mathfrak{R}_V$ with measured values, as shown in Fig. 4(b). Considering that T_c is bounded within the $2-2.3$ K interval for all samples, the voltage responsivity is almost exclusively a function of resistivity. Although $\mathfrak{R}_V$ shows a maximum for grAl sheet resistances in the range of $10-20\ \Omega$, where we would expect the detector performance to be optimal, we find it remarkable that $\mathfrak{R}_V$ does not rapidly degrade at high resistivities, several orders of magnitude greater than the ones currently used in MKID technology. This slow decrease of $\mathfrak{R}_V$ with increasing kinetic inductance opens the way for the study, and possible use, of MKIDs with very large kinetic inductance ($\alpha \approx 1$).

C. Measurement of the NEP

The opening of the optical cryostat is coupled to a matte, high-density polyethylene disk, which is cooled down by a pulse-tube cryocooler and used as a blackbody source. A layer of Eccosorb [82] absorber sponge can be manually interposed between the source and the cryostat, acting as a room-temperature blackbody. This procedure allows us to switch between a 100-K and a 300-K source. By accounting for this change in temperature, and the optical coupling between the source and the cryostat, we obtain the shift in radiant power on the sample δP_{in} [33], in the range of 0.3 pW for the H2 resonator design, and 0.1 pW for the H3 design. For each of our samples we estimate the power coupled into the MKID, $P_{\mathrm{abs}} = \delta P_{\mathrm{in}} \mathcal{A}$, by calculating the film absorptance $\mathcal{A}$, using analytical formulæ corroborated by finite-element simulations (cf. Appendix A).

Following Eq. (15), we obtain the MKID responsivity by measuring the resonant frequency shift, δf_0, when the illumination source changes from cryogenic blackbody to room temperature. The results for all samples are plotted in purple in Fig. 5(a). The brown curve in Fig. 5(a) shows the measured shift in QP density for absorbed power, $\delta x_{\mathrm{QP}}/P_{\mathrm{abs}}$, obtained by using the second and third terms of Eq. (15). The QP signal is remarkably constant for all resistivities, with an average value $\langle \delta x_{\mathrm{QP}}/P_{\mathrm{abs}} \rangle \approx (4.8 \pm 1.6) \times 10^{-4}\ \mathrm{pW}^{-1}$, indicating that the measured fluctuations in $\mathfrak{R}$ are simply due to different fundamental mode frequencies, f_0, of MKIDs in different samples.

We calculate the NSD by recording $\delta f_0(t)$ in the absence of incoming radiation, when the opening of the optical cryostat is covered. Since perfect optical sealing can not be achieved in the optical cryostat, we repeat the measurement in the dark cryostat to obtain the intrinsic noise figure of the MKIDs. The comparison between the two measured NSDs is shown in Fig. 5(b). Note that the dependence of the NSD versus resistivity shows a minimum for measurements performed in both cryostats, and the values measured in the dark are a factor of 2 lower. This nonmonotonic dependence versus normal-state resistivity of the film is correlated with the superconducting gap value reported in Fig. 5(d), which suggests quasiparticle generation-recombination as the dominant source of noise [54,55,83,84]. This would also explain the lower NSD measured in the dark cryostat, where the superior shielding and filtering results in a lower density of nonthermal QPs.

We compute the NEP as the ratio of the NSD measured in the optical cryostat and the responsivity $\mathfrak{R}$, as per Eq. (2), and we plot the results in Fig. 5(c). The dependence of the NEP versus grAl film resistivity shows a minimum at $\rho \approx 200\ \mu\Omega\,\mathrm{cm}$, corresponding to a sheet resistance $R_n \approx 100\ \Omega$, which is an order of magnitude larger than the typical values used in the MKID community [16,32,33,84–86]. We plot the values of the grAl superconducting gap Δ in

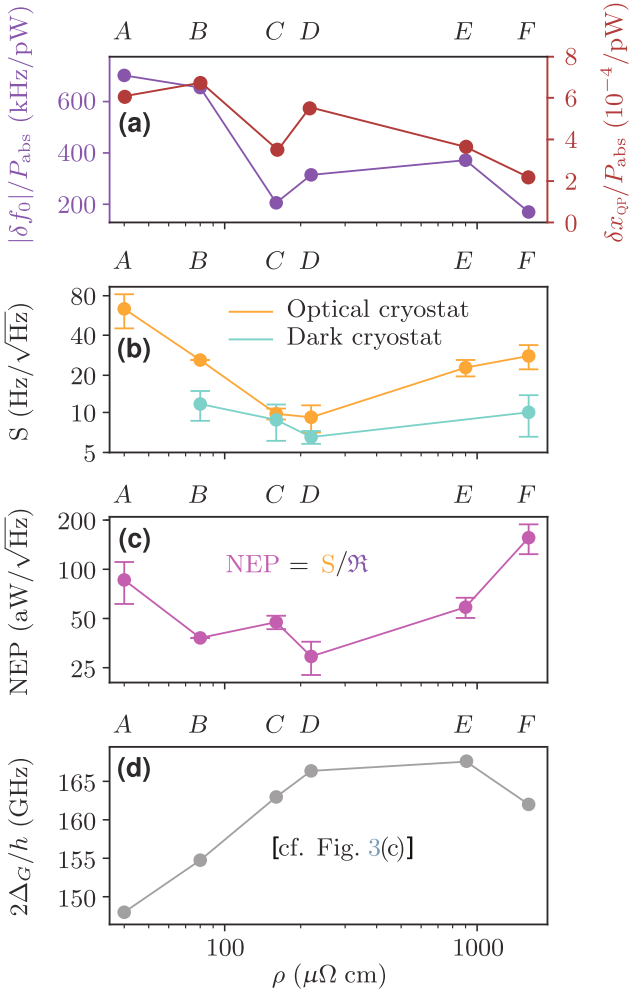

FIG. 5. Properties of grAl MKIDs as a function of film resistivity. (a) We use the measured values of $\delta f_0, f_0, \alpha$, and the estimated power absorbed by the resonators $P_{\rm abs}$, to compute the responsivity and the shift in quasiparticle density [cf. Eq. (15)], which we plot in purple and brown, respectively. (b) NSD measured for the same samples in what we denote "optical" (in orange) and "dark" (in turquoise) cryostats (cf. Sec. III), evaluated at 10 Hz. The NSD shows a minimum at $\rho \approx 200\,\mu\Omega$ cm for measurements taken in both cryostats (see the main text and Appendix B for a detailed discussion). (c) Noise-equivalent power, calculated as the ratio of measured responsivity and NSD in the optical cryostat. The resistivity dependence of the NEP is dominated by that of the NSD. (d) Measured grAl superconducting gap Δ_G, calculated from the critical temperature reported in Fig. 3(c) under the BCS assumption $\Delta = 1.76 k_B T_c$. Note that values of NEP and Δ_G are anticorrelated (see text for a detailed discussion).

Fig. 5(d) in order to highlight its anticorrelation with the NEP, as expected from the model discussed in Sec. II B [cf. Eq. (14)], under the assumption of dominating QP generation-recombination noise.

In Fig. 6 we plot the measured NEP versus Δ_G. For samples A–D, we observe an anticorrelation between the NEP and the height of the superconducting grAl gap,

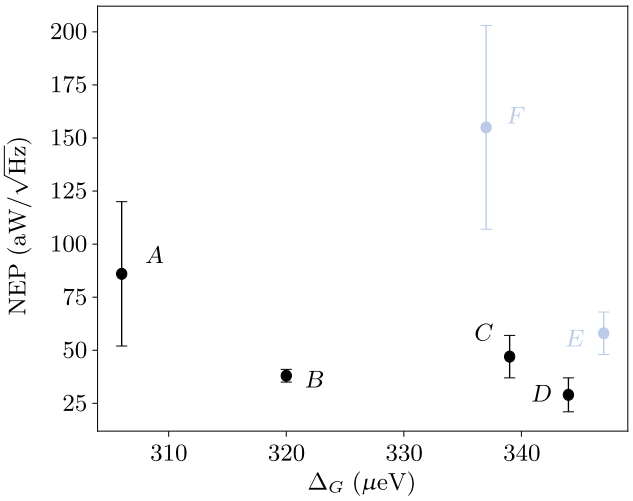

FIG. 6. Noise-equivalent power as a function of the superconducting gap of granular aluminum. Samples A–D appear to follow the anticorrelation predicted by Eq. (14)—higher granular aluminum gap results in a lower NEP. The outlier nature of samples E and F (grayed out) is addressed in the main text.

suggesting that phonon trapping in the Al ground plane plays an important role. The fact that the high-resistivity samples E and F deviate from the trend could point to an additional complexity in the quasiparticle dynamics that is currently unaccounted for, e.g., a drastically reduced diffusion length due to disorder. Furthermore, the resistivity of samples E and F is at the edge of the threshold beyond which the grAl BCS coefficient increases to about 2.1–2.2 [44–46]. While the change in the BCS factor is a small effect in itself, the underlying physics—yet to be fully understood—likely has manifold implications on quasiparticle dynamics and the corresponding noise, that go beyond our current phonon-trapping model and should be addressed in future work.

IV. CONCLUSIONS

We use granular grAl as an alternative thin-film material to fabricate MKIDs with resistivities ranging from 40 to 1600 $\mu\Omega$ cm, corresponding to kinetic inductances up to orders of magnitude higher than those found in current MKID technology. To minimize the NEP, we find an interplay between kinetic inductance fraction α and the nonlinearity limiting the maximum number of readout photons before bifurcation to $n_{\rm max}$, resulting in an optimal $\alpha = 3/4$. This value does not depend on resonator geometry, which can be optimized for maximum absorptance. In order to quantify the outcome of this interplay, we introduce the concept of voltage responsivity $\Re_V = \alpha\sqrt{n_{\rm max}}$. For $\alpha > 3/4$ we expect an increase of the NEP due the slow decrease of $\Re_V$; however, experimentally, we find the NEP to be minimum at $\alpha \approx 0.9$. This is due to the

pronounced minimum of the NSD at $\alpha \approx 0.9$, which coincides with the region of maximum grAl superconducting gap as a function of resistivity. We explain the anticorrelation between NSD and grAl gap using a phonon-trapping model in the surrounding Al ground plane. The measured NEP values for grAl MKIDs, scaled for maximum absorptance to allow for a fair comparison between different film resistivities, are in the range of 30 aW/$\sqrt{\text{Hz}}$, and are comparable to state of the art [16,32,57,65,76,83–89].

Guided by these results, future research should focus on increasing the grAl superconducting gap (e.g., using a cold deposition method as found in Ref. [90]), employing a thicker and lower gapped (e.g., titanium) ground plane, and engineering the meandered inductor geometry in order to maximize the optical impedance matching between the resonator film and the photon-collecting medium, as suggested in Ref. [91]. We believe that the flexibility, low losses, and capability of reaching high resistivities without being severely limited by the onset of nonlinearities suggest grAl as a viable candidate for future ultrasensitive MKID applications.

ACKNOWLEDGMENTS

We are grateful to A. Karpov, L. Swenson, P. de Visser, and J. Baselmans for insightful discussions, and to L. Radtke and A. Lukashenko for technical support. Facilities use is supported by the KIT Nanostructure Service Laboratory (NSL). Funding is provided by the Alexander von Humboldt Foundation in the framework of a Sofja Kovalevskaja award endowed by the German Federal Ministry of Education and Research, and by the Initiative and Networking Fund of the Helmholtz Association, within the Helmholtz Future Project Scalable solid state quantum computing. This work is partially supported by the Ministry of Education and Science of the Russian Federation in the framework of the Program to Increase Competitiveness of the NUST MISIS, Contracts No. K2-2016-063 and No. K2-2017-081.

APPENDIX A: GEOMETRY CHOICE AND IMPEDANCE MATCHING

We give a brief overview of the choice of resonator geometry, following in the footsteps of the much more detailed treatment found in Ref. [92]. The detectors used in this work are back-illuminated lumped-element resonators, composed by a meandered inductor and interdigitated capacitor, and patterned on sapphire. They offer a practical advantage over distributed resonators since the lumped-element capacitance can be swept by changing the length of the capacitor fingers, with no effect on the inductance. This is needed to obtain a fine comb of resonant frequency dips, limited only by the loaded quality factor of the resonators, which is an important consideration towards densely packed kinetic inductance arrays.

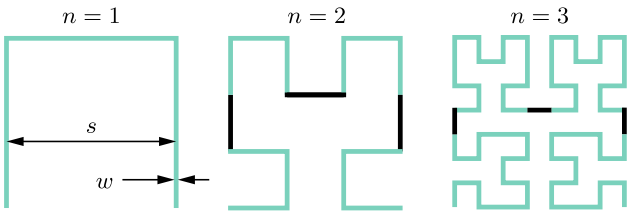

FIG. 7. First three iterations of a Hilbert fractal, i.e., Hilbert curve of the first three degrees. In green we higlight the recurrence of $(n-1)$th structures in the nth Hilbert fractal iteration, connected by black lines.

The meandered inductor is shaped as a Hilbert curve [93], shown in Fig. 7.

The nth-order fractal can be ideally decomposed into $4^n - 1$ zeroth-order structures, which are stripes of width w and length $s + w \approx s$, oriented horizontally and vertically with approximately equal distribution. The filling factor is defined as $F = w/s$. This geometry renders the detector sensitive to two polarizations at once. Increasing the degree n increases the inductance, and decreases the impedance. The two geometries we used in this work are second and third degree Hilbert curves (H2 and H3), since $n = 2$ and $n = 3$ offer a good compromise between resonant frequencies that are within the bandwidth of the readout electronics and impedances that are easily matched to the substrate. We estimate the resonator sheet resistance per square needed to assure impedance matching as

$$R_{n,\text{match}}\frac{s}{w} = \frac{Z_0}{\sqrt{\epsilon_{\text{sapphire}}}} \iff R_{n,\text{match}} \approx F \times 100\ \Omega, \tag{A1}$$

where $Z_0 \approx 377\ \Omega$ is the impedance of vacuum and $\epsilon_{\text{sapphire}}$ is the relative dielectric permittivity of the sapphire substrate. We compare this formula to finite-element simulations, showing an accuracy within 5%, and use it to estimate the detector absorptance as

$$\mathcal{A}(R_n) = \frac{|R_n - R_{n,\text{match}}|}{R_n + R_{n,\text{match}}}, \tag{A2}$$

which we then use to calculate $P_{\text{abs}} = \delta P_{\text{in}}\mathcal{A}$. The fabricated MKIDs have $\ell = 2.5$ mm, $w = 2\ \mu$m (H3) and $\ell = 1.2$ mm, $w = 12\ \mu$m (H2). Notice that H2 resonators have about three times larger surface.

APPENDIX B: NOISE SPECTRAL DENSITY

In MKIDs, the detector signal is the resonant frequency shift δf_0 caused by millimeter wave illumination. As a consequence, any fluctuation of the resonant frequency observed in the absence of incoming millimeter wave photons constitutes noise. The noise is calculated by observing

TABLE I. Geometric parameters with which Eq. (C2) is tested against the exact solution found in Ref. [94].

	Length (μm)	Width (μm)	Thickness (nm)
Span	200–2000	2–20	10–50
Step	100	2	5

the resonant frequency fluctuations over time $\delta f_0(t)$ under zero illumination condition and computing the NSD as

$$S(f) = \sqrt{\frac{|\mathcal{F}\{\delta f_0(t)\}|^2}{B}} = \frac{|\widetilde{\delta f_0}(f)|}{\sqrt{B}}, \tag{B1}$$

where B is the output bandwidth defined as $B = 1/2t_{\text{exposure}}$. We recall that the change in resonant frequency is caused by a change in kinetic inductance,

$$\delta f_0 = -f_0 \frac{\alpha}{2} \frac{\delta L_{\text{kin}}}{L_{\text{kin}}}. \tag{B2}$$

The kinetic inductance scales with the inverse of the Cooper pair density n_S, allowing one to write

$$-\frac{\delta L_{\text{kin}}}{L_{\text{kin}}} = \frac{\delta n_S}{n_S} = -\frac{\delta x_{\text{QP}}}{2}, \tag{B3}$$

where x_{QP} is the normalized grAl quasiparticle density. Under the assumption of quasiparticles dominating over other sources of noise, we can then link the fluctuations of the resonant frequency over time with fluctuations of the quasiparticle density

$$\delta f_0(t) = -\frac{\alpha}{4} f_0 \delta x_{\text{QP}}(t). \tag{B4}$$

The resonant frequency fluctuates by up to roughly 1 kHz, thus for $\alpha \approx 1$ and f_0 of the order of GHz, we obtain $\delta x_{\text{QP}} \approx 10^{-6}$, comparable to the background values recorded in Ref. [41].

APPENDIX C: KINETIC INDUCTANCE FRACTION

The kinetic inductance fraction α is defined as $\alpha = L_{\text{kin}}/(L_{\text{kin}} + L_{\text{geom}})$. The kinetic inductance of a superconducting film can be expressed as [40,42,43]

$$L_{\text{kin}} = L_{\text{kin},\square} \frac{\ell}{w} \overset{\text{Eq. (1)}}{=} \frac{0.18\hbar}{k_B} \frac{\ell}{w} \frac{R_n}{T_c}, \tag{C1}$$

where ℓ is the length, w is the width, R_n is the normal-state sheet resistance per square, and T_c is the critical temperature. In the case of the loop-free meandered inductors employed in our resonators, the geometric inductance is only given by self inductance. While the self inductance of a rectangular bar can be computed with an exact closed formula (as reported in Ref. [94]), it is lengthy and cumbersome. A much more compact formula can be found in Ref. [95], which in the thin-ribbon limit ($\ell \gg w \gg t$) reads

$$L_{\text{geom}} \approx 2 \times 10^{-7} \ell \ln\left(\frac{2\ell}{w}\right). \tag{C2}$$

We test this formula against the exact one for all combinations of ℓ, w, and t listed in Table I. Errors are always below 10%. To estimate the kinetic inductance fraction α of our resonators starting from their geometry, we combine Eqs. (C1) and (C2).

In Table II we summarize a brief literature survey of previously measured kinetic inductance fractions for MKIDs made of various thin-film materials. These values are used in Fig. 4 in the main text.

APPENDIX D: MAXIMUM NUMBER OF READOUT PHOTONS IN GRAL 1D RESONATORS

We give a brief recapitulation of the model proposed in Ref. [47]. Granular aluminum is a composite material

TABLE II. Summary of surveyed MKID parameters used in Fig. 4 in the main text, including both distributed- and lumped-element resonators.

Material	LE	R_n (Ω)	T_c (K)	α (%)	Ref.
Al	Yes	0.66	1.2	6	[11]
Al	No	0.13, 0.66, 1.3	1.2	7, 45, 63	[69]
Al	No	0.13	1.2	28	[70]
Al	No	0.13	1.2	7	[72]
Al	Yes	4	1.46	40	[73]
Al	Yes	4	1.2	50	[71]
NbTiN	No	8.75	14	9	[74]
NbTiN	No	5.6	14	35	[75]
TiN	Yes	25	4.1	74	[76]
TiN	Yes	45	2	≈ 100	[27]
WSi_2, W_3Si_5	No	45, 5.6	1.8, 4	92, 42	[77]
WSi_2, W_3Si_5	Both	7, 13, 44, 4.5	1.8, 4	43, 75, 96, 77	[31]

made of aluminum grains in a nonstoichiometric aluminum oxide matrix. The structure of grains, separated by thin insulating barriers, is modeled as a network of JJs [48–50,96]. A stripline grAl resonator, or a lumped-element grAl resonator with a thin enough meandered inductor, can be considered as a one-dimensional chain of effective JJs, which allows the resonator self-Kerr [97] nonlinearity to be derived

$$K_{11} = \mathcal{C}\pi e a \frac{\omega_0^2}{j_c V}, \tag{D1}$$

where a is the characteristic size of an aluminum grain, $V = \ell w t$ is the volume of the resonator, j_c is the critical current density, e is the electron charge, $\omega_0 = 2\pi f_0$ is the resonant frequency, and $\mathcal{C}$ is a geometric parameter of order unity, which in our case is $\mathcal{C} = 3/16$. The maximum number of photons in the resonator at bifurcation is [64]

$$n_{\max} = \frac{\kappa}{\sqrt{3}K_{11}}, \tag{D2}$$

where $\kappa = f_0/Q_{\text{tot}}$ is the instantaneous bandwidth of the resonator. The total kinetic inductance of the JJ array is $L_{\text{kin}} = L_J \times \ell/a$, where L_J is the inductance of a single effective JJ, allowing us to write

$$j_c = \frac{\ell\hbar}{2eaL_{\text{kin}}wt}. \tag{D3}$$

Under the assumption of strongly overcoupled resonators ($Q_{\text{tot}} \approx Q_c$), and kinetic inductance dominating over the geometric inductance ($1/f_0 \approx 2\pi\sqrt{L_{\text{kin}}C}$), we can use Eqs. (D1) to (D3) to write

$$n_{\max} = \frac{4\ell^2\hbar\sqrt{C}}{3\sqrt{3}Q_c(\pi e a)^2\sqrt{L_{\text{kin}}}}. \tag{D4}$$

APPENDIX E: SUMMARY OF RESONATOR PARAMETERS

We present a summary of the material properties of the fabricated samples in Table III.

TABLE III. Summary of the material properties of the grAl films presented in this work.

Sample	R_n ($\Omega/\square$)	ρ ($\mu\Omega$ cm)	$L_{\text{kin},\square}$ (pH/$\square$)	T_c (K)	α (%)	NEP (aW/$\sqrt{Hz}$)
A	20	40	16	2.02	90	86 ± 34
B	40	80	32	2.11	95	38 ± 3
C	80	160	64	2.23	97	47 ± 10
D	110	220	88	2.27	98	29 ± 8
E	450	900	360	2.29	100	58 ± 10
F	800	1600	640	2.22	100	155 ± 48

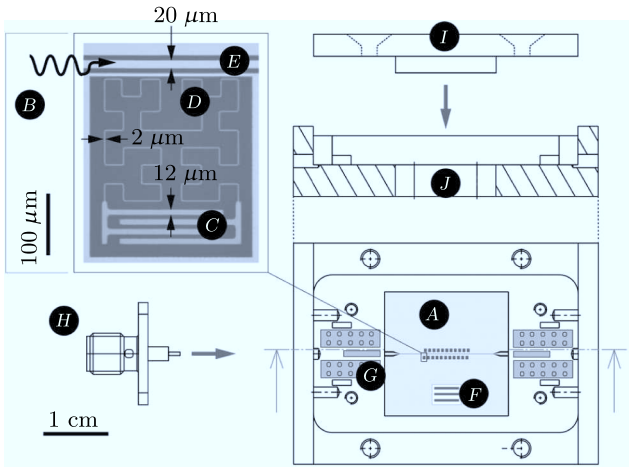

FIG. 8. Technical drawing of the aluminum sample holder. The inset shows an optical image of a single H3 resonator.

APPENDIX F: SAMPLE-HOLDER DESIGN

We show a technical drawing of the aluminum sample holder in Fig. 8. The inset enlarges the sapphire chip (A) to show one of the 22 resonators (B), where we highlight the interdigitated capacitor (C), meandered third-degree Hilbert curve inductor (D) and CPW feedline (E). Note that H2 resonators have a meander width of 12 μm. The chip also hosts test stripes (F) used for room-temperature dc measurements of the sheet resistance (more stripes are present on the wafer prior to dicing). The feedline is wire bonded to the printed circuit boards (G) that couple to coaxial connectors (H). The sample holder is closed with a solid aluminum lid (I), with an aperture on the backside (J), allowing for millimeter wave illumination.

APPENDIX G: PHOTON NUMBER CALIBRATION IN THE DARK CRYOSTAT

We give a brief description of the dark-cryostat experimental setup, and of the method used to estimate the number of photons circulating in a resonator. As schematically shown in Fig. 9, the sample under test is thermally anchored to the dilution stage of a cryostat, and we perform rf transmission measurements. We use a vector network analyzer (VNA) to generate the input tone and to analyze the output. We add room temperature and cryogenic attenuators to the input line, with a typical total attenuation in the range of -90 dB. A number of fixed attenuators and a low pass filter are used at different temperature stages of the cryostat to prevent rf heating and to thermalize the input rf field. Once the rf signal is transmitted through the sample, an isolator is used to prevent back-propagating noise from the amplifiers. The signal is filtered and travels through superconducting cables (green) before being amplified by a HEMT amplifier at 4 K, and a room-temperature amplifier.

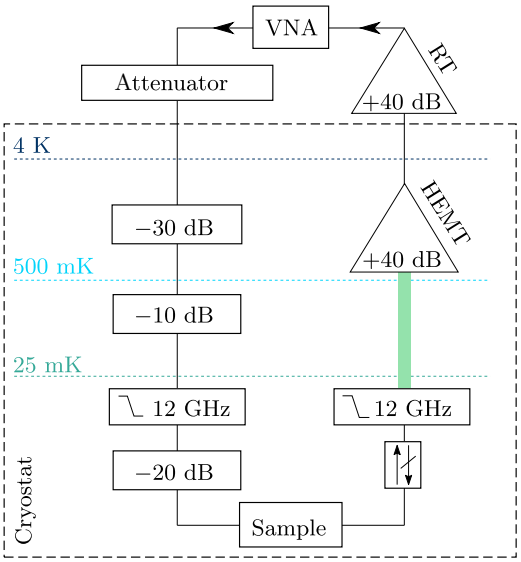

FIG. 9. Schematic diagram of the measurement setup in the dark cryostat.

We estimate the drive power at the sample-holder input, P_{cold}, simply by adding all known attenuation sources on the input line. For a strongly overcoupled resonator ($Q_{\text{tot}} \approx Q_c$), we estimate the average number of photons using the following expression [98]:

$$\bar{n} = P_{\text{cold}} \frac{2Q_c}{\hbar\omega_0^2}. \tag{G1}$$

For example, our typical values are $Q_c = 10^5$ and $f_0 = 5$ GHz, resulting in a one-photon regime for $P_{\text{cold}} \approx -150$ dBm. The attenuation figures of the employed components and of the microwave lines, as well as the amplifiers gain, can only be coarsely estimated. For this reason, we expect our photon number estimation to be precise within an order of magnitude. Furthermore, as reported in the main text, this method appears to systematically underestimate the number of photons circulating in the resonators by a factor 2, which might be due to overestimation of the input line attenuation.

[1] Peter K. Day, Henry G. LeDuc, Benjamin A. Mazin, Anastasios Vayonakis, and Jonas Zmuidzinas, A broadband superconducting detector suitable for use in large arrays, Nature **425**, 817 (2003).

[2] A Monfardini *et al.*, Latest NIKA results and the NIKA-2 project, J. Low Temp. Phys. **176**, 787 (2014).

[3] J. Schlaerth, A. Vayonakis, P. Day, J. Glenn, J. Gao, S. Golwala, S. Kumar, H. LeDuc, B. Mazin, J. Vaillancourt, and J. Zmuidzinas, A millimeter and submillimeter kinetic inductance detector camera, J. Low Temp. Phys. **151**, 684 (2008).

[4] Philip R. Maloney, Nicole G. Czakon, Peter K. Day, Thomas P. Downes, Ran Duan, Jiansong Gao, Jason Glenn, Sunil R. Golwala, Matt I. Hollister, Henry G. LeDuc, Benjamin A. Mazin, Sean G. McHugh, Omid Noroozian, Hien T. Nguyen, Jack Sayers, James A. Schlaerth, Seth Siegel, John E. Vaillancourt, Anastasios Vayonakis, Philip Wilson, and Jonas Zmuidzinas, in *Millimeter, Submillimeter, and Far-Infrared Detectors and Instrumentation for Astronomy V* (International Society for Optics and Photonics, San Diego, California, United States, 2010), Vol. 7741, p. 77410F.

[5] E. Shirokoff, P. S. Barry, M. Bradford, G. Chattopadhyay, P. Day, S. Doyle, S. Hailey-Dunsheath, M. I. Hollister, A. Kovács, C. McKenney, H. G. Leduc, N. Llombart, D. P. Marrone, P. Mauskopf, R. O'Brient, S. Padin, T. Reck, L. J. Swenson, and J. Zmuidzinas, in *Millimeter, Submillimeter, and Far-Infrared Detectors and Instrumentation for Astronomy VI* (International Society for Optics and Photonics, Amsterdam, Netherlands, 2012), Vol. 8452, p. 84520R.

[6] B. A. Mazin, S. R. Meeker, M. J. Strader, P. Szypryt, D. Marsden, J. C. van Eyken, G. E. Duggan, A. B. Walter, G. Ulbricht, M. Johnson, B. Bumble, K. O'Brien, and C. Stoughton, ARCONS: A 2024 pixel optical through near-IR cryogenic imaging spectrophotometer, Publ. Astron. Soc. Pacific **125**, 1348 (2013).

[7] S. Oguri, J. Choi, T. Damayanthi, M. Hattori, M. Hazumi, H. Ishitsuka, K. Karatsu, S. Mima, M. Minowa, T. Nagasaki, C. Otani, Y. Sekimoto, O. Tajima, N. Tomita, M. Yoshida, and E. Won, GroundBIRD: Observing cosmic microwave polarization at large angular scale with kinetic inductance detectors and high-speed rotating telescope, J. Low Temp. Phys. **184**, 786 (2016).

[8] Orlando Quaranta, T. W. Cecil, Lisa Gades, Benjamin Mazin, and Antonino Miceli, X-ray photon detection using superconducting resonators in thermal quasi-equilibrium, Supercond. Sci. Technol. **26**, 105021 (2013).

[9] P. Szypryt, B. A. Mazin, B. Bumble, H. G. Leduc, and L. Baker, Ultraviolet, optical, and near-IR microwave kinetic inductance detector materials developments, IEEE Trans. Appl. Superconduct. **25**, 1 (2015).

[10] E. S. Battistelli, F. Bellini, C. Bucci, M. Calvo, L. Cardani, N. Casali, M. G. Castellano, I. Colantoni, A. Coppolecchia, C. Cosmelli, A. Cruciani, P. de Bernardis, S. Di Domizio, A. D'Addabbo, M. Martinez, S. Masi, L. Pagnanini, C. Tomei, and M. Vignati, Calder: Neutrinoless double-beta decay identification in TeO_2 bolometers with kinetic inductance detectors, Eur. Phys. J. C **75**, 353 (2015).

[11] L. Cardani, I. Colantoni, A. Cruciani, S. Di Domizio, M. Vignati, F. Bellini, N. Casali, M. G. Castellano, A. Coppolecchia, C. Cosmelli, and C. Tomei, Energy resolution and efficiency of phonon-mediated kinetic inductance detectors for light detection, Appl. Phys. Lett. **107**, 093508 (2015).

[12] L. Cardani, N. Casali, I. Colantoni, A. Cruciani, F. Bellini, M. G. Castellano, C. Cosmelli, A. D'Addabbo, S. Di Domizio, M. Martinez, C. Tomei, and M. Vignati, High sensitivity phonon-mediated kinetic inductance detector with combined amplitude and phase read-out, Appl. Phys. Lett. **110**, 033504 (2017).

[13] A. Patel, A. Brown, W. Hsieh, T. Stevenson, S. H. Moseley, K. U-yen, N. Ehsan, E. Barrentine, G. Manos, and E. J. Wollack, Fabrication of MKIDs for the microspec spectrometer, IEEE Trans. Appl. Supercond. **23**, 2400404 (2013).

[14] T. Matsumura *et al.*, Mission design of LiteBIRD, J. Low Temp. Phys. **176**, 733 (2014).

[15] Matthew Griffin, J. Baselmans, A. Baryshev, Simon Doyle, M. Grim, Peter Hargrave, T. Klapwijk, J. Martin-Pintado, A. Monfardini, A. Neto, H. Steenbeek, I. Walker, K. Wood, A. D'Addabbo, P. Barry, A. Bideau, B. Blázquez, J. Bueno, M. Calvo, J. L. Costa-Kramer, L. Ferrari, A. Gómez-Gutiérrez, J. Goupy, N. Llombart, and S. Yates, in *Millimeter, Submillimeter, and Far-Infrared Detectors and Instrumentation for Astronomy VIII* (International Society for Optics and Photonics, Edinburgh, United Kingdom, 2016), Vol. 9914, p. 991407f.

[16] J. Baselmans, J. Bueno, O. Yurduseven, S. Yates, N. Llombart, V. Murugesan, D. J. Thoen, A. Baryshev, and A. Neto, in *2016 41st International Conference on Infrared, Millimeter, and Terahertz Waves (IRMMW-THz)* (IEEE, Copenhagen, Denmark, 2016), p. 1.

[17] G. J. Grabovskij, L. J. Swenson, O. Buisson, C. Hoffmann, A. Monfardini, and J.-C. Villégier, In situ measurement of the permittivity of helium using microwave NbN resonators, Appl. Phys. Lett. **93**, 134102 (2008).

[18] O. Dupré, A. Benoît, M. Calvo, A. Catalano, J. Goupy, C. Hoarau, T. Klein, K. Le Calvez, B. Sacépé, A. Monfardini, and F. Levy-Bertrand, Tunable sub-gap radiation detection with superconducting resonators, Supercond. Sci. Technol. **30**, 045007 (2017).

[19] L. J. Swenson, A. Cruciani, A. Benoit, M. Roesch, C. S. Yung, A. Bideaud, and A. Monfardini, High-speed phonon imaging using frequency-multiplexed kinetic inductance detectors, Appl. Phys. Lett. **96**, 263511 (2010).

[20] D. C. Moore, S. R. Golwala, P. K. Day, H. G. LeDuc, and J. Zmuidzinas, Position and energy-resolved particle detection using phonon-mediated microwave kinetic inductance detectors, Appl. Phys. Lett. **100**, 232601 (2012).

[21] Simon Doyle, Philip Mauskopf, J. Naylon, Adrian Porch, and C. Duncombe, Lumped element kinetic inductance detectors, J. Low Temp. Phys. **151**, 530 (2008).

[22] K. Hayashi, A. Saito, T. Sawada, Y. Ogawa, K. Nakajima, H. Yamada, S. Ariyoshi, and S. Ohshima, Microwave characteristics of microwave kinetic inductance detectors using rewound spiral resonators array, Phys. Procedia **45**, 213 (2013).

[23] Masato Naruse, Yutaro Sekimoto, Takashi Noguchi, Akihira Miyachi, Kenichi Karatsu, Tom Nitta, Masakazu Sekine, Yoshinori Uzawa, Tohru Taino, and Hiroaki Myoren, Optical efficiencies of lens-antenna coupled kinetic inductance detectors at 220 GHz, IEEE Trans. Terahertz Sci. Technol. **3**, 180 (2013).

[24] Y. Sekimoto, S. Sekiguchi, S. Shu, M. Sekine, T. Nitta, M. Naruse, A. Dominjon, T. Hasebe, W. Shan, T. Noguchi, A. Miyachi, M. Mita, and S. Kawasaki, Design of corrugated-horn-coupled MKID focal plane for cmb b-mode polarization, (2016).

[25] Peter K. Day *et al.*, Optics for music: A new (sub)millimeter camera for the caltech submillimeter observatory, (2010).

[26] J. Gao, M. R. Vissers, M. O. Sandberg, F. C. S. da Silva, S. W. Nam, D. P. Pappas, D. S. Wisbey, E. C. Langman, S. R. Meeker, B. A. Mazin, H. G. Leduc, J. Zmuidzinas, and K. D. Irwin, A titanium-nitride near-infrared kinetic inductance photon-counting detector and its anomalous electrodynamics, Appl. Phys. Lett. **101**, 142602 (2012).

[27] L. J. Swenson, P. K. Day, B. H. Eom, and H. G. Leduc, Operation of a titanium nitride superconducting microresonator detector in the nonlinear regime, J. Appl. Phys. **113**, 104501 (2013).

[28] J. Bueno, P. C. J. J. Coumou, G. Zheng, P. J. De Visser, T. M. Klapwijk, E. F. C Driessen, S. Doyle, and J. J. A Baselmans, Anomalous response of superconducting titanium nitride resonators to terahertz radiation, Appl. Phys. Lett. **105**, 192601 (2014).

[29] A. Saito, K. Nakajima, K. Hayashi, Y. Ogawa, Y. Okuyama, D. Oka, S. Ariyoshi, H. Yamada, T. Taino, C. Otani, J. Bae, and S. Ohshima, Relationship between loaded quality factor and responsivity for NbN-based MKIDs using dual-function spiral strip, IEEE Trans. Appl. Supercond. **25**, 1 (2015).

[30] P. Szypryt, B. A. Mazin, G. Ulbricht, B. Bumble, S. R. Meeker, C. Bockstiegel, and A. B. Walter, High quality factor platinum silicide microwave kinetic inductance detectors, Appl. Phys. Lett. **109**, 151102 (2016).

[31] Thomas Cecil, Antonino Miceli, Orlando Quaranta, Chian Liu, Daniel Rosenmann, Sean McHugh, and Benjamin Mazin, Tungsten silicide films for microwave kinetic inductance detectors, Appl. Phys. Lett. **101**, 032601 (2012).

[32] R. M. J. Janssen, J. J. A. Baselmans, S. J. C. Yates, A. M. Baryshev, and T. M. Klapwijk, in *Millimeter, Submillimeter, and Far-Infrared Detectors and Instrumentation for Astronomy VII* (International Society for Optics and Photonics, San Diego, California, United States, 2014), Vol. 9153, p. 91530T.

[33] A. Catalano, J. Goupy, H. Le Sueur, A. Benoit, O. Bourrion, M. Calvo, A. D'addabbo, L. Dumoulin, F. Levy-Bertrand, J. Macías-Pérez, S. Marnieros, N. Ponthieu, and A. Monfardini, Bi-layer kinetic inductance detectors for space observations between 80–120 GHz, Astron. Astrophys. **580**, A15 (2015).

[34] J. Hubmayr, J. Beall, D. Becker, H.-M. Cho, M. Devlin, B. Dober, C. Groppi, G. C. Hilton, K. D. Irwin, D. Li, P. Mauskopf, D. P. Pappas, J. Van Lanen, M. R. Vissers, Y. Wang, L. F. Wei, and J. Gao, Photon-noise limited sensitivity in titanium nitride kinetic inductance detectors, Appl. Phys. Lett. **106**, 073505 (2015).

[35] Agnes Dominjon, Masakazu Sekine, Kenichi Karatsu, Takashi Noguchi, Yutaro Sekimoto, Shibo Shu, Shigeyuchi Sekiguchi, and Tom Nitta, Study of superconducting bilayer for microwave kinetic inductance detectors for astrophysics, IEEE Trans. Appl. Supercond. **26**, 1 (2016).

[36] L. Cardani, N. Casali, A. Cruciani, H. le Sueur, M. Martinez, F. Bellini, M. Calvo, M. G. Castellano, I. Colantoni, C. Cosmelli, A. D'Addabbo, S. Di Domizio, J. Goupy, L. Minutolo, A. Monfardini, and M. Vignati, Al/Ti/Al phonon-mediated KIDs for UV–vis light detection over large areas, Supercond. Sci. Technol. **31**, 075002 (2018).

[37] B. Abeles, Roger W. Cohen, and G. W. Cullen, Enhancement of superconductivity in metal films, Phys. Rev. Lett. **17**, 632 (1966).

[38] G. Deutscher, M. Gershenson, E. Grünbaum, and Y. Imry, Granular superconducting films, J. Vac. Sci. Technol. **10**, 697 (1973).

[39] L. Sun, L. DiCarlo, M. D. Reed, G. Catelani, Lev S. Bishop, D. I. Schuster, B. R. Johnson, Ge. A. Yang, L. Frunzio, L. Glazman, M. H. Devoret, and R. J. Schoelkopf, Measurements of Quasiparticle Tunneling Dynamics in a Band-Gap-Engineered Transmon Qubit, Phys. Rev. Lett. **108**, 230509 (2012).

[40] H. Rotzinger, S. T. Skacel, M. Pfirrmann, J. N. Voss, J. Münzberg, S. Probst, P. Bushev, M. P. Weides, A. V. Ustinov, and J. E. Mooij, Aluminium-oxide wires for superconducting high kinetic inductance circuits, Supercond. Sci. Technol. **30**, 025002 (2016).

[41] Lukas Grünhaupt, Nataliya Maleeva, Sebastian T. Skacel, Martino Calvo, Florence Levy-Bertrand, Alexey V. Ustinov, Hannes Rotzinger, Alessandro Monfardini, Gianluigi Catelani, and Ioan M. Pop, Loss Mechanisms and Quasiparticle Dynamics in Superconducting Microwave Resonators made of Thin-Film Granular Aluminum, Phys. Rev. Lett. **121**, 117001 (2018).

[42] Michael Tinkham, *Introduction to Superconductivity* (Courier Corporation, 2004), 2nd ed., p. 98.

[43] Anthony J. Annunziata, Daniel F. Santavicca, Luigi Frunzio, Gianluigi Catelani, Michael J. Rooks, Aviad Frydman, and Daniel E. Prober, Tunable superconducting nanoinductors, Nanotechnology **21**, 445202 (2010).

[44] Uwe S. Pracht, Nimrod Bachar, Lara Benfatto, Guy Deutscher, Eli Farber, Martin Dressel, and Marc Scheffler, Enhanced cooper pairing versus suppressed phase coherence shaping the superconducting dome in coupled aluminum nanograins, Phys. Rev. B **93**, 100503 (2016).

[45] Aviv Glezer Moshe, Eli Farber, and Guy Deutscher, Optical conductivity of granular aluminum films near the metal to insulator transition: Evidence for a BCS-BEC crossover, arXiv:1901.02814 (2019).

[46] F. Levy-Bertrand, T. Klein, T. Grenet, O. Dupré, A. Benoît, A. Bideaud, O. Bourrion, M. Calvo, A. Catalano, A. Gomez, J. Goupy, L. Grünhaupt, U. v. Luepke, N. Maleeva, F. Valenti, I. M. Pop, and A. Monfardini, Electrodynamics of granular aluminum from superconductor to insulator: Observation of collective superconducting modes, Phys. Rev. B **99**, 094506 (2019).

[47] Nataliya Maleeva, Lukas Grünhaupt, T. Klein, F. Levy-Bertrand, O. Dupré, M. Calvo, F. Valenti, P. Winkel, F. Friedrich, W. Wernsdorfer, A. V. Ustinov, A. Monfardini, M. V. Fistul, and I. M. Pop, Circuit quantum electrodynamics of granular aluminum resonators, Nat. Commun. **9**, 3889 (2018).

[48] J. Bourassa, F. Beaudoin, Jay M. Gambetta, and A. Blais, Josephson-junction-embedded transmission-line resonators: From Kerr medium to in-line transmon, Phys. Rev. A **86**, 013814 (2012).

[49] G. Tancredi, G. Ithier, and P. J. Meeson, Bifurcation, mode coupling and noise in a nonlinear multimode superconducting microwave resonator, Appl. Phys. Lett. **103**, 063504 (2013).

[50] T. Weißl, B. Küng, E. Dumur, A. K. Feofanov, I. Matei, C. Naud, O. Buisson, F. W. J. Hekking, and W. Guichard, Kerr coefficients of plasma resonances in Josephson junction chains, Phys. Rev. B **92**, 104508 (2015).

[51] Clemens Müller, Jared H. Cole, and Jürgen Lisenfeld, Towards understanding two-level-systems in amorphous solids-insights from quantum devices, arXiv:1705.01108 (2017).

[52] Hélène le Sueur, Artis Svilans, Nicolas Bourlet, Anil Murani, Laurent Bergé, Louis Dumoulin, and Philippe Joyez, Microscopic charged fluctuators as a limit to the coherence of disordered superconductor devices, arXiv:1810.12801 (2018).

[53] Benjamin A.Mazin, "Microwave kinetic inductance detectors," Tech. Rep. (2005).

[54] A. V. Sergeev and M. Yu. Reizer, Photoresponse mechanisms of thin superconducting films and superconducting detectors, Int. J. Mod. Phys. B **10**, 635 (1996).

[55] A. V. Sergeev, V. V. Mitin, and B. S. Karasik, Ultrasensitive hot-electron kinetic-inductance detectors operating well below the superconducting transition, Appl. Phys. Lett. **80**, 817 (2002).

[56] Alain Benoit, Aurelien Bideaud, Olivier Bourrion, Andrea Catalano, Martino Calvo, Antonio D'Addabbo, Simon Doyle, Johannes Goupy, Helene Le Sueur, Juan Macias-Perez, Alessandro Monfardini, and Jochem Baselmans, Lumped element kinetic inductance detectors for space applications, (2016).

[57] J. J. A. Baselmans, J. Bueno, S. J. C. Yates, A. Endo, D. J. Thoen, P. J. de Visser, R. M. J. Janssen, V. Murugesan, E. F. C. Driessen, G. Coiffard, J. Martin-Pintado, P. Hargrave, and M. Griffin, A kilo-pixel imaging system for future space based far-infrared observatories using microwave kinetic inductance detectors, A&A **601**, A89 (2017).

[58] K. Karatsu, A. Endo, J. Bueno, P. J. de Visser, R. Barends, D. J. Thoen, V. Murugesan, N. Tomita, and J. J. A. Baselmans, Mitigation of cosmic ray effect on microwave kinetic inductance detector arrays, Appl. Phys. Lett. **114**, 032601 (2019).

[59] S. B. Kaplan, C. C. Chi, D. N. Langenberg, Jhy-Jiun Chang, S. Jafarey, and D. J. Scalapino, Quasiparticle and phonon lifetimes in superconductors, Phys. Rev. B **14**, 4854 (1976).

[60] N. Bachar, S. Lerer, S. Hacohen-Gourgy, B. Almog, and G. Deutscher, Kondo-like behavior near the metal-to-insulator transition of nanoscale granular aluminum, Phys. Rev. B **87**, 214512 (2013).

[61] Shachar Lerer, Nimrod Bachar, Guy Deutscher, and Yoram Dagan, Nernst effect beyond the coherence critical field of a nanoscale granular superconductor, Phys. Rev. B **90**, 214521 (2014).

[62] N. Bachar, S. Lerer, A. Levy, S. Hacohen-Gourgy, B. Almog, H. Saadaoui, Z. Salman, E. Morenzoni, and G. Deutscher, Mott transition in granular aluminum, Phys. Rev. B **91**, 041123 (2015).

[63] Georg Duffing, *Erzwungene Schwingungen bei veränderlicher Eigenfrequenz und ihre technische Bedeutung* (F. Vieweg & sohn, Braunschweig, Germany, 1918), p. 41.

[64] Christopher Eichler and Andreas Wallraff, Controlling the dynamic range of a josephson parametric amplifier, EPJ Quantum Technol. **1**, 2 (2014).

[65] P. J. De Visser, J. J. A. Baselmans, Juan Bueno, Nuria Llombart, and T. M. Klapwijk, Fluctuations in the electron system of a superconductor exposed to a photon flux, Nat. Commun. **5**, 3130 (2014).

[66] P. J. De Visser, D. J. Goldie, P. Diener, J. J. A. Baselmans, and T. M. Klapwijk, Evidence of a Nonequilibrium Distribution of Quasiparticles in the Microwave Response of a Superconducting Aluminum Resonator, Phys. Rev. Lett. **112**, 047004 (2014).

[67] A. V. Semenov, I. A. Devyatov, P. J. de Visser, and T. M. Klapwijk, Coherent excited states in superconductors due to a microwave field, Phys. Rev. Lett. **117**, 047002 (2016).

[68] S Probst, F. B. Song, P. A. Bushev, A. V. Ustinov, and M Weides, Efficient and robust analysis of complex scattering data under noise in microwave resonators, Rev. Sci. Instrum. **86**, 024706 (2015).

[69] Jiansong Gao, *The Physics of Superconducting Microwave Resonators* (California Institute of Technology, California Institute of Technology, 2008).

[70] J. Gao, J. Zmuidzinas, B. A. Mazin, P. K. Day, and H. G. Leduc, Experimental study of the kinetic inductance fraction of superconducting coplanar waveguide, Nucl. Instrum. Methods Phys. Res. Sect. A: Accelerators, Spectrometers, Detectors Assoc. Equip. **559**, 585 (2006).

[71] P. D. Mauskopf, S. Doyle, P. Barry, S. Rowe, A. Bidead, P. A. R. Ade, C. Tucker, E. Castillo, A. Monfardini, J. Goupy, and M. Calvo, Photon-noise limited performance in aluminum lekids, J. Low Temp. Phys. **176**, 545 (2014).

[72] Benjamin A. Mazin, Bruce Bumble, Peter K. Day, Megan E. Eckart, Sunil Golwala, Jonas Zmuidzinas, and Fiona A. Harrison, Position sensitive x-ray spectrophotometer using microwave kinetic inductance detectors, Appl. Phys. Lett. **89**, 222507 (2006).

[73] H. McCarrick, D. Flanigan, G. Jones, B. R. Johnson, P. Ade, D. Araujo, K. Bradford, R. Cantor, G. Che, P. Day, S. Doyle, H. Leduc, M. Limon, V. Luu, P. Mauskopf, A. Miller, T. Mroczkowski, C. Tucker, and J. Zmuidzinas, Horn-coupled, commercially-fabricated aluminum lumped-element kinetic inductance detectors for millimeter wavelengths, Rev. Sci. Instrum. **85**, 123117 (2014).

[74] R. M. J. Janssen, J. J. A. Baselmans, A. Endo, L. Ferrari, S. J. C. Yates, A. M. Baryshev, and T. M. Klapwijk, High optical efficiency and photon noise limited sensitivity of microwave kinetic inductance detectors using phase readout, Appl. Phys. Lett. **103**, 203503 (2013).

[75] S. J. C. Yates, J. J. A. Baselmans, A. Endo, R. M. J. Janssen, L. Ferrari, P. Diener, and A. M. Baryshev, Photon noise limited radiation detection with lens-antenna coupled microwave kinetic inductance detectors, Appl. Phys. Lett. **99**, 073505 (2011).

[76] Henry G. Leduc, Bruce Bumble, Peter K. Day, Byeong Ho Eom, Jiansong Gao, Sunil Golwala, Benjamin A. Mazin, Sean McHugh, Andrew Merrill, David C. Moore, Omid Noroozian, Anthony D. Turner, and Jonas Zmuidzinas, Titanium nitride films for ultrasensitive microresonator detectors, Appl. Phys. Lett. **97**, 102509 (2010).

[77] Orlando Quaranta, Thomas W. Cecil, and Antonino Miceli, Tungsten silicide alloys for microwave kinetic inductance detectors, IEEE Trans. Appl. Supercond. **23**, 2400104 (2013).

[78] Lukas Grünhaupt, Uwe von Lüpke, Daria Gusenkova, Sebastian T. Skacel, Nataliya Maleeva, Steffen Schlör, Alexander Bilmes, Hannes Rotzinger, Alexey V. Ustinov, Martin Weides, and Ioan M. Pop, An argon ion beam milling process for native AlOx layers enabling coherent superconducting contacts, Appl. Phys. Lett. **111**, 072601 (2017).

[79] Wenyuan Zhang, K. Kalashnikov, Wen-Sen Lu, P. Kamenov, T. DiNapoli, and M. E. Gershenson, Microresonators fabricated from high-kinetic-inductance aluminum films, Phys. Rev. Applied **11**, 011003 (2019).

[80] I. Nsanzineza and B. L. T. Plourde, Trapping a Single Vortex and Reducing Quasiparticles in a Superconducting Resonator, Phys. Rev. Lett. **113**, 117002 (2014).

[81] Simon Gustavsson, Fei Yan, Gianluigi Catelani, Jonas Bylander, Archana Kamal, Jeffrey Birenbaum, David Hover, Danna Rosenberg, Gabriel Samach, Adam P. Sears, Steven J. Weber, Jonilyn L. Yoder, John Clarke, Andrew J. Kerman, Fumiki Yoshihara, Yasunobu Nakamura, Terry P. Orlando, and William D. Oliver, Suppressing relaxation in superconducting qubits by quasiparticle pumping, **354**, 1573 (2016).

[82] Emerson & Cuming Microwave Products, Inc., "ECCOSO RB AN absorber": http://www.eccosorb.com/products-eccosorb-an.htm.

[83] P. J. De Visser, J. J. A. Baselmans, P. Diener, S. J. C. Yates, A. Endo, and T. M. Klapwijk, Number Fluctuations of Sparse Quasiparticles in a Superconductor, Phys. Rev. Lett. **106**, 167004 (2011).

[84] P. J. De Visser, J. J. A. Baselmans, P. Diener, S. J. C. Yates, A. Endo, and T. M. Klapwijk, Generation-recombination noise: The fundamental sensitivity limit for kinetic inductance detectors, J. Low Temp. Phys. **167**, 335 (2012).

[85] J. Bueno, O. Yurduseven, S. J. C. Yates, N. Llombart, V. Murugesan, D. J. Thoen, A. M. Baryshev, A. Neto, and J. J. A. Baselmans, Full characterisation of a background limited antenna coupled kid over an octave of bandwidth for thz radiation, Appl. Phys. Lett. **110**, 233503 (2017).

[86] D. Flanigan, H. McCarrick, G. Jones, B. R. Johnson, M. H. Abitbol, P. Ade, D. Araujo, K. Bradford, R. Cantor, G. Che, P. Day, S. Doyle, C. B. Kjellstrand, H. Leduc, M. Limon, V. Luu, P. Mauskopf, A. Miller, T. Mroczkowski, C. Tucker, and J. Zmuidzinas, Photon noise from chaotic and coherent millimeter-wave sources measured with horn-coupled, aluminum lumped-element kinetic inductance detectors, Appl. Phys. Lett. **108**, 083504 (2016).

[87] Francesco Giazotto, Tero T. Heikkilä, Giovanni PieroPepe, Panu Helistö, Arttu Luukanen, and Jukka P. Pekola, Ultrasensitive proximity josephson sensor with kinetic inductance readout, Appl. Phys. Lett. **92**, 162507 (2008).

[88] J. Baselmans, S. J. C Yates, R. Barends, Y. J. Y. Lankwarden, J. R. Gao, H. Hoevers, and T. M. Klapwijk, Noise and sensitivity of aluminum kinetic inductance detectors for sub-mm astronomy, J. Low Temp. Phys. **151**, 524 (2008).

[89] M. Calvo *et al.*, The NIKA2 instrument, a dual-band kilopixel KID array for millimetric astronomy, J. Low Temp. Phys. **184**, 816 (2016).

[90] Roger W. Cohen and B. Abeles, Superconductivity in granular aluminum films, Phys. Rev. **168**, 444 (1968).

[91] Christopher M. McKenney, Henry G. Leduc, Loren J. Swenson, Peter K. Day, Byeong H. Eom, and Jonas Zmuidzinas, in *Millimeter, Submillimeter, and Far-Infrared Detectors and Instrumentation for Astronomy VI*

(International Society for Optics and Photonics, 2012), Vol. 8452, p. 84520S.

[92] Markus Rösch, *Development of Lumped Element Kinetic Inductance Detectors for mm-Wave Astronomy at the IRAM 30 m Telescope* (KIT Scientific Publishing, Karlsruhe, Germany, 2014), Vol. 12.

[93] David Hilbert, Über die stetige abbildung einer line auf ein flächenstück, Mathematische Annalen **38**, 459 (1891).

[94] Zygmunt Piatek and Bernard Baron, Exact closed form formula for self inductance of conductor of rectangular cross section, Prog. Electromagn. Res. **26**, 225 (2012).

[95] Frederick Emmons Terman, *Radio Engineers' Handbook* (McGraw-Hill Book, New York, United States, 1943).

[96] Carsten Hutter, Erik A. Tholén, Kai Stannigel, Jack Lidmar, and David B. Haviland, Josephson junction transmission lines as tunable artificial crystals, Phys. Rev. B **83**, 014511 (2011).

[97] Daniel F. Walls and Gerard J. Milburn, *Quantum Optics* (Springer Science & Business Media, Berlin, Germany, 2007).

[98] S. J. Weber, K. W. Murch, and D. H. Slichter, Single crystal silicon capacitors with low microwave loss in the single photon regime, Appl. Phys. Lett. **98**, 172510 (2011).